**SUPPLEMENTARY INFORMATION for**

# Highly sensitive active pixel image sensor array driven by large-area bilayer $MoS_2$ transistor circuitry


## Authors

*Seongin Hong[†,1], Nicolò Zagni[†,2], Sooho Choo[†,1], Na Liu[†,1], Seungho Baek[1], Arindam Bala[1], Hocheon Yoo[3], Byung Ha Kang[4], Hyun Jae Kim[4], Hyung Joong Yun[5], Muhammad Ashraful Alam[*,6] and Sunkook Kim[*,1]*

## Affiliations

[1] School of Advanced Materials Science and Engineering, Sungkyunkwan University, Suwon 440-746, Republic of Korea

[2] Department of Engineering "Enzo Ferrari" (DIEF), University of Modena and Reggio Emilia, Modena 41125, Italy

[3] Department of Electronic Engineering, Gachon University, Seognam 13120, Republic of Korea

[4] School of Electrical and Electronic Engineering, Yonsei University, Seoul 03722, Republic of Korea

[5] Research Center for Materials Analysis, Korea Basic Science Institute (KBSI), Daejeon 34133, Republic of Korea.

[6] School of Electrical and Computer Engineering, Purdue University, West Lafayette, Indiana 47907, USA

*Corresponding author. Email: alam@purdue.edu, intel0616@gmail.com

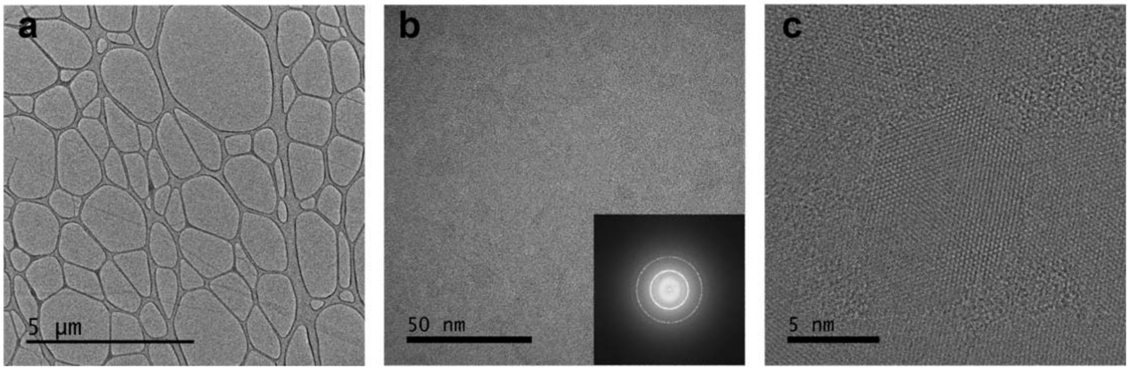


**Supplementary Figure 1 I TEM images of bilayer $MoS_2$ films. a,** Low-magnification and **b and c,** high-magnification TEM images. The inset of **b** is a FFT pattern corresponding to the TEM image.

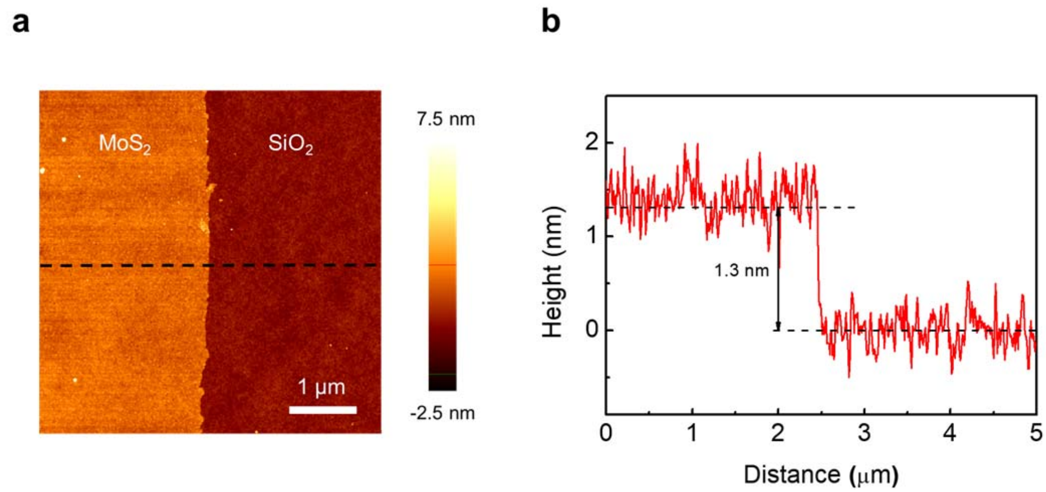


**Supplementary Figure 2 l Thickness of a bilayer $MoS_2$ film directly synthesized on a $SiO_2$/Si substrate using the two-step growth method. a**, AFM image of the bilayer $MoS_2$ film. **b**. Line profile data of dark-dashed line in the AFM image. The thickness of the $MoS_2$ film was estimated to be approximately 1.3 nm.

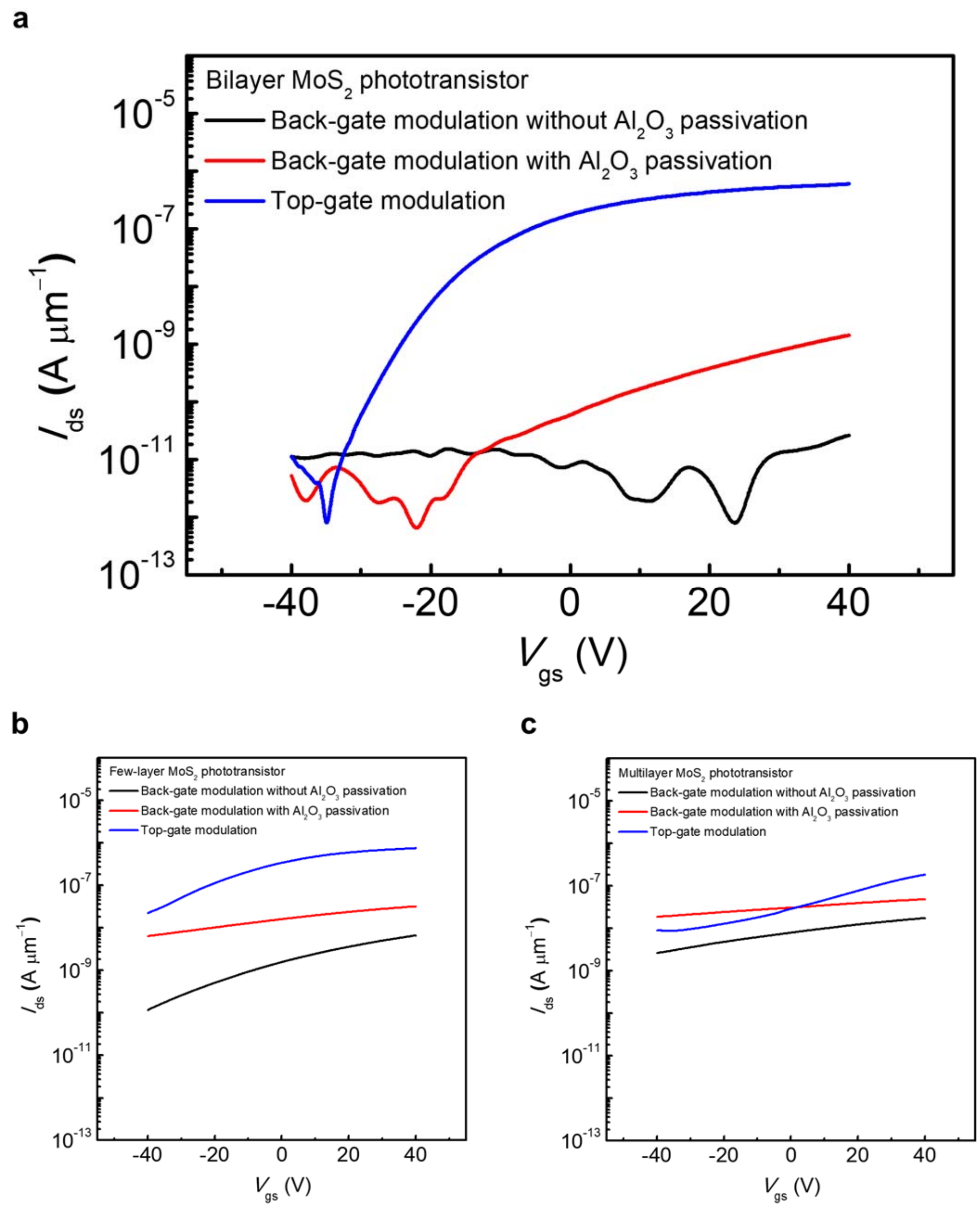


**Supplementary Figure 3 | Comparison of the electrical properties of $MoS_2$ phototransistors.** Transfer curves of **a**, bilayer, **b**, few-layer, and **c**, multilayer $MoS_2$ phototransistor under back-gate modulation without $Al_2O_3$ passivation (black line), back-gate modulation with $Al_2O_3$ passivation (red line), and top-gate modulation (blue line).

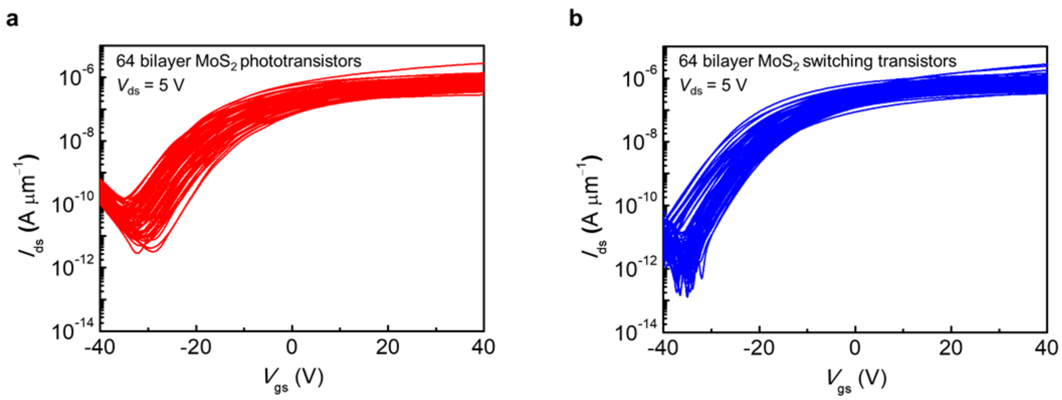


**Supplementary Figure 4 l Electrical properties of all the phototransistors and switching transistors in the 8 × 8 active image sensor array with a bilayer $MoS_2$ film.** Transfer characteristics of **a**, 64 phototransistors and **b**, 64 switching transistors at $V_{ds}$ = 5 V.

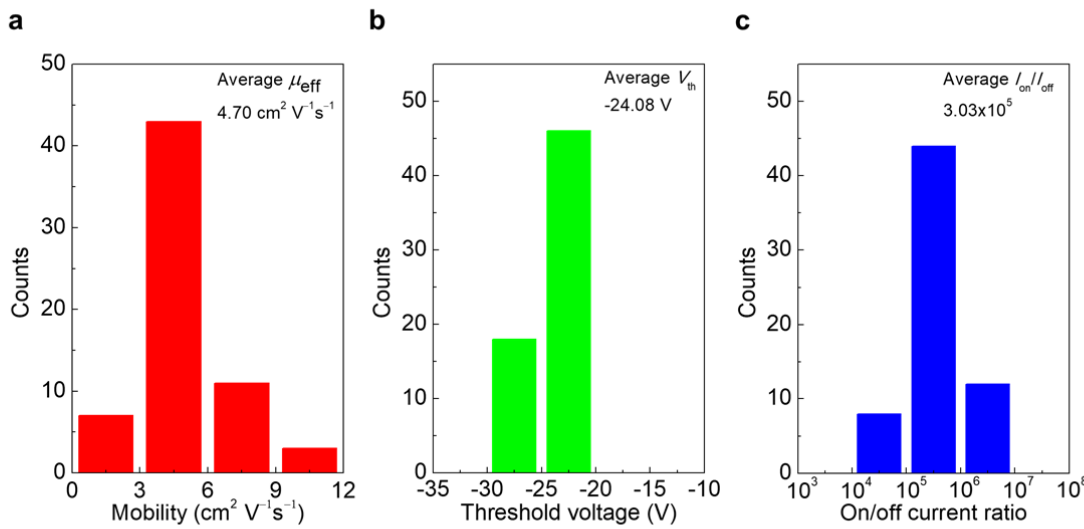


**Supplementary Figure 5 | Statistical analysis of switching transistors in the bilayer $MoS_2$ image sensor array.** Histograms of **a**, field effect mobility (average $\mu_{eff}$ = 4.70 $cm^2 V^{-1} s^{-1}$), **b**, threshold voltage (average $V_{th}$ = −24.08 V), and **c**, on/off current ratio (average $I_{on}/I_{off}$ = 3.03 × $10^5$) of the 64 $MoS_2$ switching transistors.

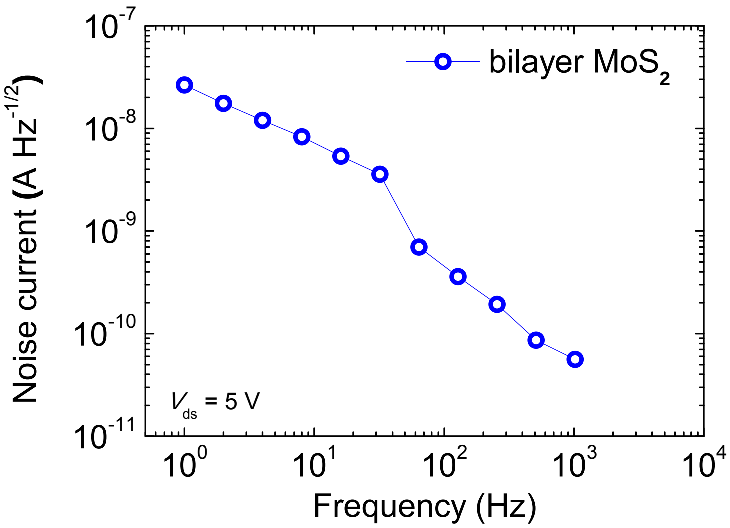


**Supplementary Figure 6 l** Measured noise current as a function of frequency for the bilayer $MoS_2$ phototransistors at $V_{ds}$ = 5 V.

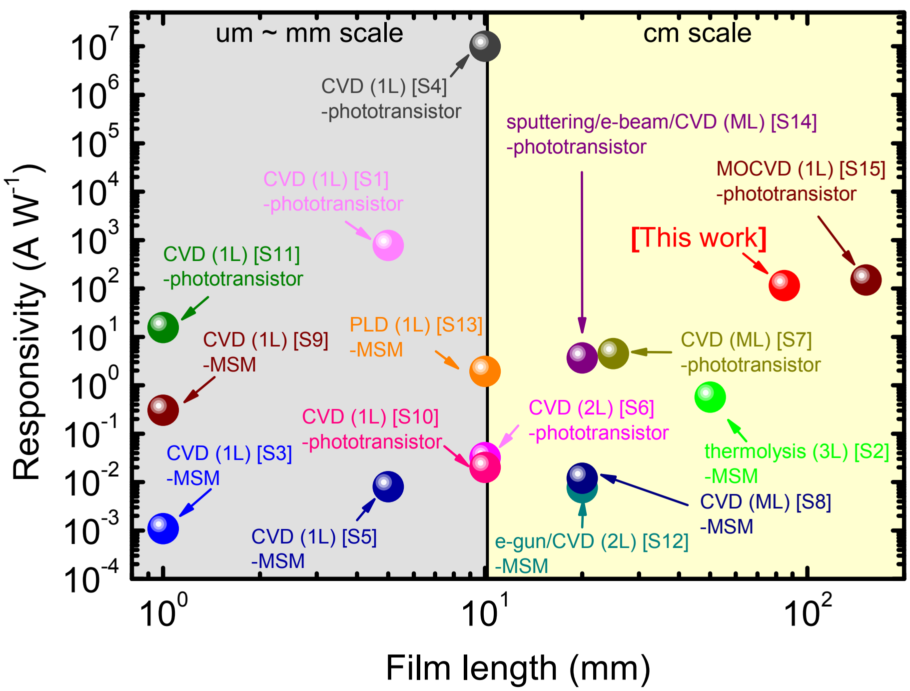


**Supplementary Figure 7 |** Comparison of the photoresponsivity of the proposed phototransistor based on the synthesized $MoS_2$ with those of previous studies.

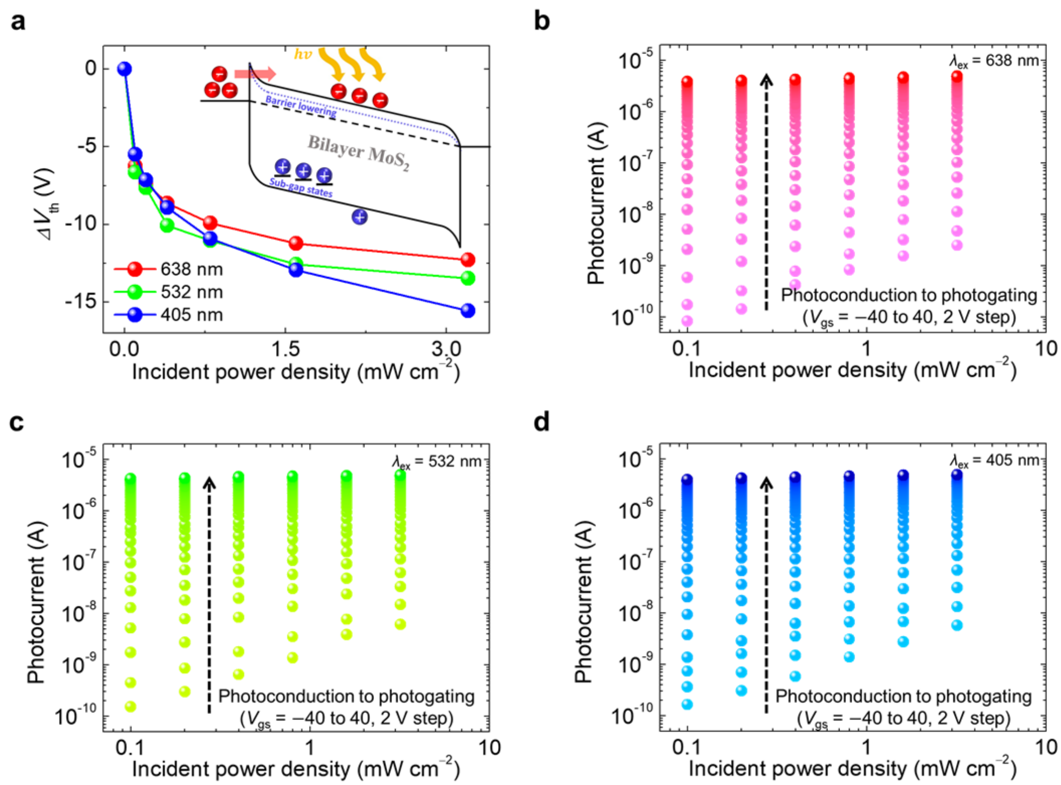


**Supplementary Figure 8 l Threshold voltage and photocurrent variation of the bilayer $MoS_2$ phototransistor as a function of $P_{inc}$ under RGB light illumination.** **a**, $\Delta V_{th}$–$P_{inc}$ curves of the $MoS_2$ phototransistor under RGB light illumination. The inset is the energy band diagram of the $MoS_2$ phototransistor, indicating the mechanism of the PG effect. $I_{ph}$ - $P_{inc}$ curves of the $MoS_2$ phototransistor at various $V_{gs}$ under **b**, red **c**, green and **d**, blue light illumination.

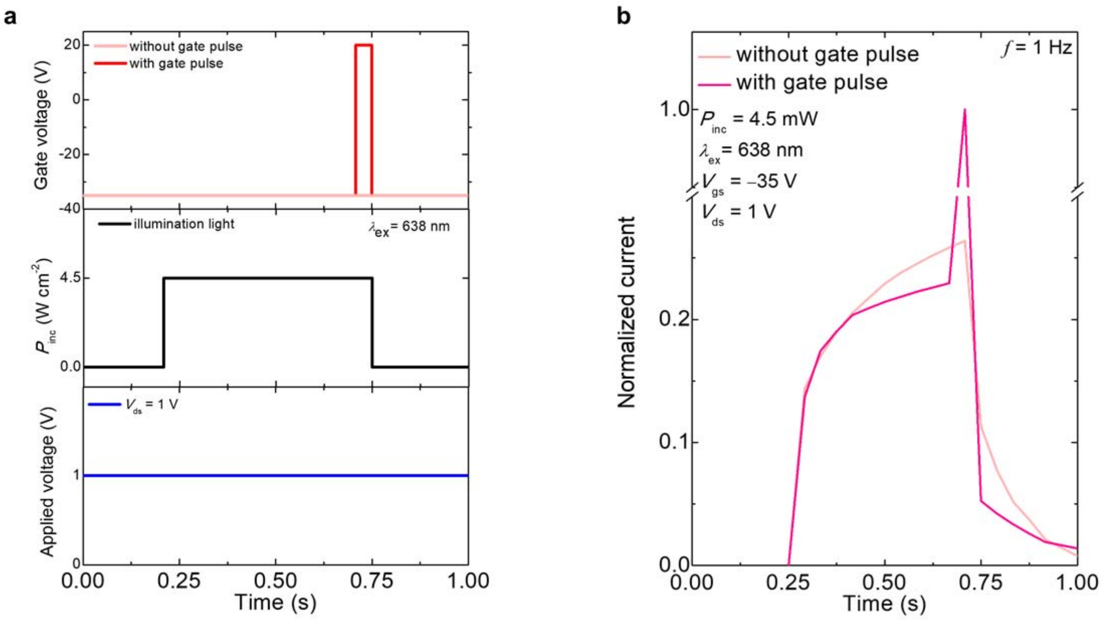


**Supplementary Figure 9 l Photoswitching characteristics with gate pulse of a bilayer $MoS_2$ phototransistor in the image sensor array. a**, Measurement conditions for photoswitching properties with gate pulse. Switching curves were measured at $V_{ds}$ = 1 V, $V_{gs}$ = −35 V and $P_{inc}$ = 4.5 mW cm$^{-2}$ with illumination frequency of 1 Hz. The applied gate pulse is 20 V with a width of 40 ms. **b**, Time resolved photoresponsive characteristics of the bilayer $MoS_2$ phototransistor under temporal light illumination with $\lambda_{ex}$ = 638 nm without and with gate voltage pulse. The fall time is improved from 104.80 ms to 23.99 ms.

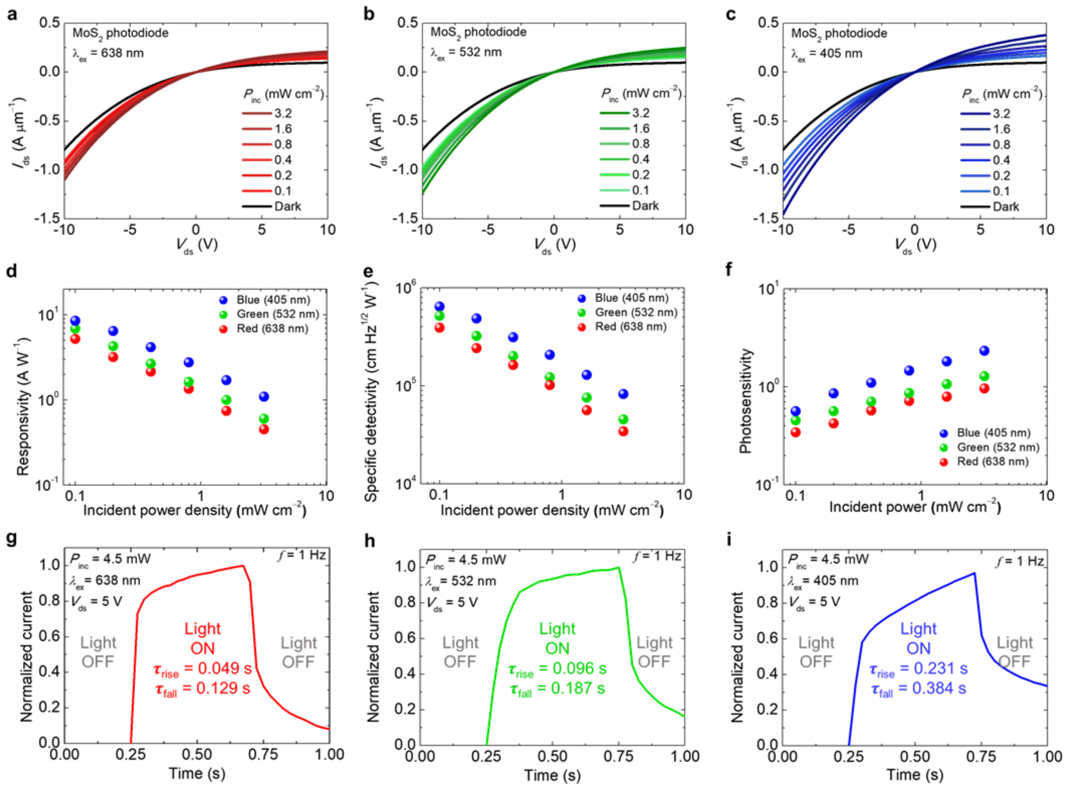


**Supplementary Figure 10 | Photoresponsive characteristics of a bilayer $MoS_2$ photodetector without a top-gate electrode in the image sensor array.** *I*–*V* curves of a photodetector without a top-gate electrode based on a bilayer $MoS_2$ channel under **a**, red **b**, green and **c**, blue light illumination with various incident power densities ($\lambda_{ex}$ = 638 nm (R), 532 nm (G), 405 nm (B), and $P_{inc}$ = 0.1, 0.2, 0.4, 0.8, 1.6, 3.2 mW $cm^{-2}$). **d**, Photoresponsivity, **e**, specific detectivity, and **f**, photosensitivity of the $MoS_2$ photodetector without a top-gate electrode calculated from Supplementary Fig. 10a–c. **g–i**, Photoswitching characteristics of the $MoS_2$ phototransistor under temporal light illumination with $\lambda_{ex}$ = 638, 532, and 405 nm, respectively. All the switching curves were measured at $V_{ds}$ = 5 V and $P_{inc}$ = 4.5 mW $cm^{-2}$ with the illumination frequency of 1 Hz. The rise and fall times were calculated as the times taken for the current to change from 20–80% and 80–20% of the maximum current, respectively.

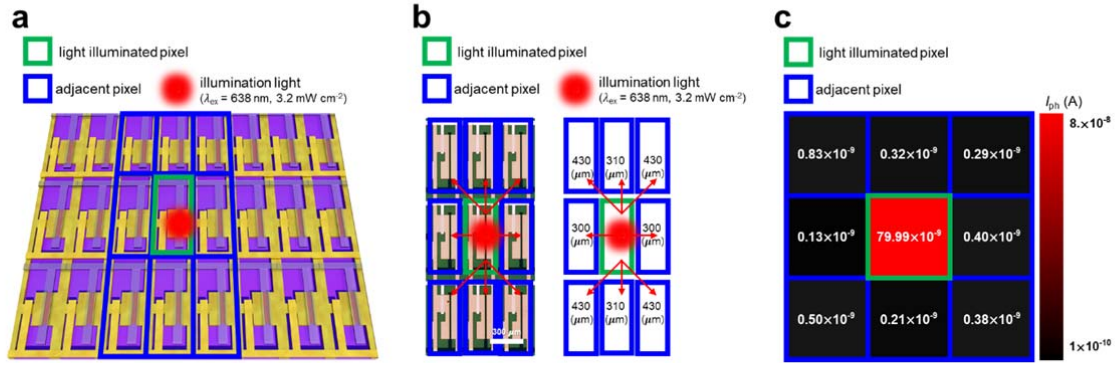


**Supplementary Figure 11 | Cross-talk characterization of a light-illuminated pixel and its adjacent pixels.** **a**, Schematic of the light-illuminated pixel and adjacent pixels. **b**, Optical microscopy image of the light-illuminated pixel and adjacent pixels. The specific length between channel of phototransistors in the light-illuminated pixel and that of phototransistors in adjacent pixels (top, bottom: 310 $\mu$m, right, left: 300 $\mu$m, and diagonal: 430 $\mu$m, respectively). **c**, Photocurrent mapping of the light-illuminated pixel and adjacent pixels under red light ($\lambda_{ex}$ = 638 nm) with $P_{inc}$ of 3.2 mW cm$^{-2}$ at $V_{gs}$ = -35 V and $V_{ds}$ = 1 V.

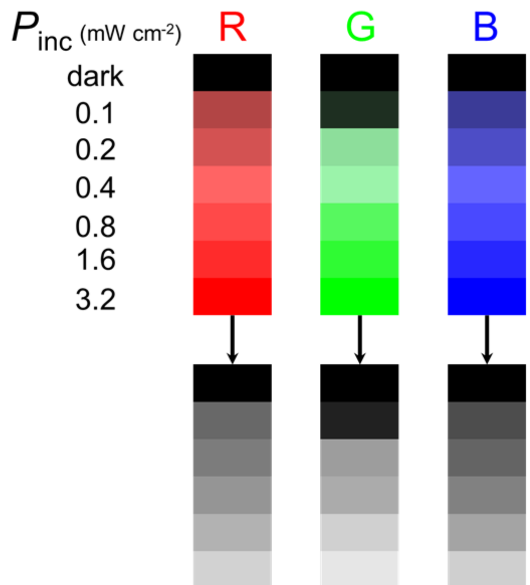


**Supplementary Figure 12 l** Grayscale image of a phototransistor in the image sensor array under various incident power density. The RGB color scale split by various incident power density and their grayscale equivalences, respectively.

**Supplementary Table 1 l** Comparison of the performance of the proposed photodetector with those of previous studies

| Method | Layer | Large area | Spectrum range (λ) | Photo responsivity | Configuration | Active pixel array | Year | Ref. |
|---|---|---|---|---|---|---|---|---|
| CVD | 1L | × | 532 nm | 780 A $W^{-1}$ in ambient air | Phototransistor $SiO_2$ - Si | × | 2013 | S1 |
| Two-step (thermolysis process) | 3L | ○ | 532 nm | 0.57 A $W^{-1}$ | MSM | × | 2013 | S2 |
| CVD | 1L | × | 488 nm<br>514.5 nm | 1.1 mA $W^{-1}$ | MSM | × | 2014 | S3 |
| CVD | 1L | ○ | 650 nm | $10^7$ A $W^{-1}$ | Phototransistor $SiO_2$ - Si | × | 2014 | S4 |
| CVD | 1L | × | 475 nm<br>535 nm<br>575 nm<br>630 nm | 7.7 mA $W^{-1}$ | MSM | × | 2015 | S5 |
| CVD | 2L | ○ | 650 nm | 32 mA $W^{-1}$ | Phototransistor $SiO_2$ - Si | × | 2016 | S6 |
| CVD | 6L | ○ | 515 nm | 4–5 A $W^{-1}$ | Phototransistor $Al_2O_3$ - Ti/Au | × | 2017 | S7 |
| CVD | Multilayer | ○ | 405 nm<br>532 nm | 12.1 mA $W^{-1}$ | MSM | × | 2017 | S8 |
| CVD | 1L | × | 575 nm | 308 mA $W^{-1}$ | Homojunction photodiode | × | 2017 | S9 |
| CVD | 1L | ○ | 405 nm<br>520 nm<br>658 nm<br>780 nm | 20 mA $W^{-1}$ | Phototransistor PVP - PEDOT:PSS | × | 2017 | S10 |
| CVD | 1L | × | 632 nm | 15.6 A $W^{-1}$ | Phototransistor $SiO_2$ - Si | × | 2017 | S11 |
| E-gun evaporator/CVD | 2L | ○ | 408 nm<br>515 nm<br>640 nm | 8.0 mA $W^{-1}$ | MSM | × | 2019 | S12 |
| Pulsed laser deposition (PLD) | 1–5L | ○ | 300 nm<br>~<br>800 nm | 1.96 A $W^{-1}$ | MSM | × | 2019 | S13 |
| Sputtering/ e-beam irradiation/ CVD | Multilayer | ○ | 405 nm | 3.7 A $W^{-1}$ | Phototransistor $SiO_2$ - Si | × | 2020 | S14 |
| MOCVD | 1L | ○ | 532 nm | 150 A $W^{-1}$ | Phototransistor $SiO_2$ - Si | ○ | 2020 | S15 |
| Two-step (sputtering/CVD) | 2L | ○ | 405 nm<br>532 nm<br>638 nm | 119.16 A $W^{-1}$<br>116.70 A $W^{-1}$<br>109.00 A $W^{-1}$ | Phototransistor $Al_2O_3$ - IZO | ○ | 2021 | This work |

**Supplementary Table 2 I** Comparison with the response time of the phototransistor in image sensor array without and with gate pulse.

| | $\tau_r$ | $\tau_f$ | Gate pulse (V, ms) |
|---|---|---|---|
| Bilayer $MoS_2$ phototransistor | 169.19 ms | 104.8 ms | NA |
| | 111.11 ms | 22.99 ms | 20, 40 |

## Supplementary Note 1 I Simulations

The 2-D numerical simulations under illumination and in the dark are performed with a commercial software[S16]. Carrier transport was treated with the drift-diffusion formalism (see Supplementary Table 3 for the equations set). With this approach Poisson equation and continuity equations are solved self-consistently for each applied bias (in terms of gate-to-source and drain-to-source voltage) to obtain the electrostatic potential and the carriers' concentration. The light source is considered to be ideal, i.e., providing constant generation rates, for simplicity.

**Supplementary Table 3 I** Drift-Diffusion Equations used to model electrostatics and carrier transport in the device simulations.

| | |
|---|---|
| Poisson Equation | $\nabla \cdot (\varepsilon \nabla \psi) = -q(p - n + N_D - N_A)$ |
| Continuity Equation | $\mp \nabla J_{n,p} = q(G_{n,p} - R_{n,p})$ |
| Drift-Diffusion Equations | $J_n = \mu_n n(-\nabla\psi) + D_n \nabla n$<br>$J_p = \mu_p p(-\nabla\psi) - D_p \nabla p$ |
| Recombination Equation | $R_{n,p} = \dfrac{np - n_i^2}{\tau_n(p + p_1) + \tau_p(n + n_1)}$ |

The device structure implemented in the simulator is schematically represented in Fig. 1, with indication of device dimensions. The geometrical parameters adopted in the simulations are collected in Supplementary Table 4.

**Supplementary Table 4 I** Geometrical dimensions adopted in the device simulations.

| Symbol | Description | Parameter value |
|---|---|---|
| $L_G$ | Gate Length | 15 µm |
| $W_G$ | Gate Width | 250 µm |
| $t_{ox}$ | Gate Oxide Thickness | 80 nm |
| $t_{chan}$ | $MoS_2$ Channel Thickness | 2 nm |
| $t_{box}$ | Buried Oxide Thickness | 300 nm |

Supplementary Table 5 collects the $MoS_2$ material parameters used in the simulations. Supplementary Table 6 includes additional device parameters used in the simulations. Schottky barriers are considered at the boundaries of the $MoS_2$ layer with the source and drain contacts. SHR and Radiative recombination in the semiconductor layer are also taken into account. The $Al_2O_3$ is the gate oxide material ($\varepsilon_r \sim 7$).

Simulation results with no traps included are shown in Supplementary Figure 13a. No appreciable negative $V_{th}$ shift can be observed in this case in contrast with the case with traps included, see Supplementary Figure 13b. This confirms the hypothesis concerning PG as the dominant effect determining photoresponsivity. Simulated band diagrams at different $V_{gs}$ are shown in Supplementary Figure 14 under light illumination (i.e., $P_{inc} \approx 10^{-1}$ mW cm$^{-2}$) with (Supplementary Figures 14a-e) and without traps (Supplementary Figures 14f-j) included in the simulations. When light generates electron-hole pairs the excess holes get trapped into the trap level at 0.2 eV above $E_V$ causing $V_{th}$ to shift. This is illustrated by Supplementary Figure 15, that shows the trapped charge density ($N_T^+$) at different $V_{gs}$ in the dark and with light illumination, clearly indicating that more charge gets trapped in the latter case than in the former.

**Supplementary Table 5 |** $MoS_2$ material parameters[S17].

| **Symbol** | **Description** | **Parameter value** |
|---|---|---|
| $E_G$ | Band Gap | 1.4 eV |
| $\chi$ | Electron Affinity | 4.4 eV |
| $\varepsilon_r$ | $MoS_2$ Relative Dielectric Constant | 5 |
| $N_C$ | Effective Density of States in the Conduction Band | $1.12 \times 10^{19}$ $cm^{-3}$ |
| $N_V$ | Effective Density of States in the Valence Band | $2.54 \times 10^{19}$ $cm^{-3}$ |
| $n_i$ | Intrinsic Carrier Concentration | $2.93 \times 10^{7}$ $cm^{-3}$ |
| $N_A$ | Doping Concentration (p-type) | $5.0 \times 10^{19}$ $cm^{-3}$ |
| $\mu_{n,p}$ | Carriers' Mobility | 5 $cm^2$ $V^{-1}$ $s^{-1}$ |
| $\tau_{n,p}$ | Carriers' Lifetime | 1 μs |

**Supplementary Table 6 |** Additional device parameters used in the simulations.

| **Symbol** | **Description** | **Parameter value** |
|---|---|---|
| $\varepsilon_{r,ox}$ | Relative Dielectric Constant ($Al_2O_3$) | 7 |
| $\Phi_G$ | Gate Contact Work-Function | 5 eV (IZO) |
| $\Phi_{S,D}$ | Source, Drain Contacts Work-Function | 5 eV (Gold) |

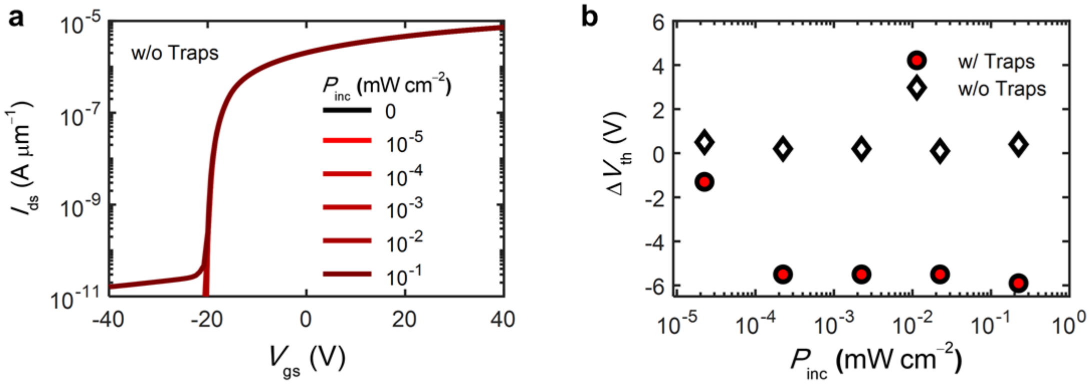


**Supplementary Figure 13 l Additional simulation results. a,** Simulated $I_{ds}$-$V_{gs}$ with no traps included under light illumination, for different incident power densities ($P_{inc}$). **b,** Comparison of the Threshold Voltage Shift ($\Delta V_{th}$) vs $P_{inc}$ extracted from the $I_{ds}$-$V_{gs}$ simulation with and without traps included.

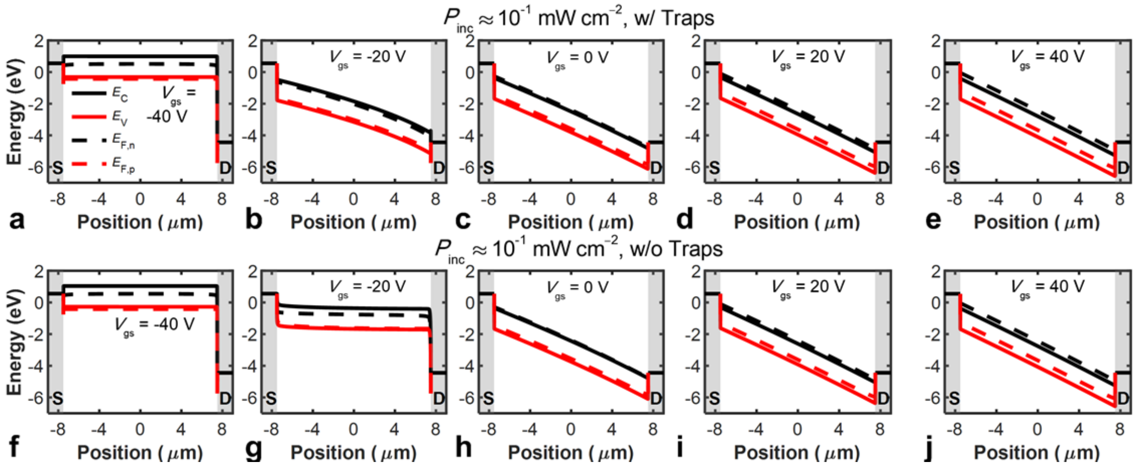


**Supplementary Figure 14 l** Simulated energy band diagrams for different $V_{gs}$ = (-40, -20, 0, 20, 40) V under light illumination ($P_{inc} \approx 10^{-1}$ mW cm$^{-2}$) with (**a-e**) and without traps (**f-j**).

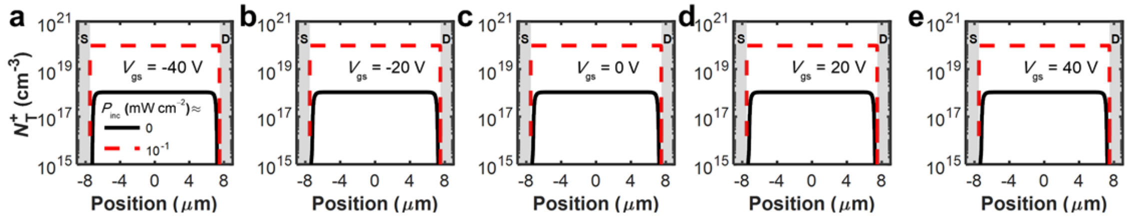


**Supplementary Figure 15 | Trapped charge density. a-e,** Trapped charge density ($N_T^+$) for different $V_{gs}$ = (-40, -20, 0, 20, 40) V in the dark ($P_{inc}$ = 0 mW cm$^{-2}$, black lines). and under light illumination ($P_{inc} \approx 10^{-1}$ mW cm$^{-2}$, red-dashed lines).

**Supplementary References**


S1. Zhang, W. et al. High□gain phototransistors based on a CVD $MoS_2$ monolayer. *Adv. Mater.* **25**, 3456-3461 (2013).

S2. Tsai, D.-S. et al. Few-layer $MoS_2$ with high broadband photogain and fast optical switching for use in harsh environments. *ACS Nano* **7**, 3905-3911 (2013).

S3. Perea-López, N. et al. CVD-grown monolayered $MoS_2$ as an effective photosensor operating at low-voltage. *2D Mater.* **1**, 011004 (2014).

S4. Zhang, W. *et al.* Ultrahigh-gain photodetectors based on atomically thin graphene-$MoS_2$ heterostructures. *Sci. Rep.* **4**, 1-8 (2014).

S5. Le, C. T. et al. Photosensitivity Study of Metal-Semiconductor-Metal Photodetector Based on Chemical Vapor Deposited Monolayer $MoS_2$. *J. Nanosci. Nanotechnol.* **15**, 8133-8138 (2015).

S6. Chen, C. et al. Large-scale synthesis of a uniform film of bilayer $MoS_2$ on graphene for 2D heterostructure phototransistors. *ACS Appl. Mater. Interfaces* **8**, 19004-19011 (2016).

S7. Choi, C. et al. Human eye-inspired soft optoelectronic device using high-density $MoS_2$-graphene curved image sensor array. *Nat. Commun.* **8**, 1-11 (2017).

S8. Lee, S. H. et al. Large□area growth of multi□layered $MoS_2$ for violet (～405 nm) photodetector applications. *Phys. Status Solidi A* **214**, 1700221 (2017).

S9. Zhang, X. et al. Poly(4-styrenesulfonate)-induced sulfur vacancy self-healing strategy for monolayer $MoS_2$ homojunction photodiode. *Nat. Commun.* **8**, 1-8 (2017).

S10. Kim, T.-Y. et al. Transparent large-area $MoS_2$ Phototransistors with inkjet-printed components on flexible platforms. *ACS Nano* **11**, 10273-10280 (2017).

S11. Nie, C. et al. Ultrafast growth of large-area monolayer $MoS_2$ film via gold foil assistant CVD for a highly sensitive photodetector. *Nanotechnology* **28**, 275203 (2017).

S12. Chen, S.-W. H. et al. Enhanced wavelength-selective photoresponsivity with a $MoS_2$ bilayer grown conformally on a patterned sapphire substrate. *J. Mater. Chem. C* **7**, 1622-1629 (2019).

S13. Jiao, L. et al. Layer-dependent photoresponse of 2D $MoS_2$ films prepared by pulsed laser deposition. *J. Mater. Chem. C* **7**, 2522-2529 (2019).

S14. Park, H. et al. Exceptionally Uniform and Scalable Multilayer $MoS_2$ Phototransistor Array Based on Large-Scale $MoS_2$ Grown by RF Sputtering, Electron Beam Irradiation, and Sulfurization. *ACS Appl. Mater. Interfaces* **12**, 20645-20652 (2020).

S15. Jang, H. *et al.* An atomically thin optoelectronic machine vision processor. *Adv. Mater.* **32**, 2002431 (2020).

S16. Synopsys Sentaurus SDevice Manual (O-2018.06) (2018).

S17. K.-C. Wang *et al.* Control of interlayer physics in 2H transition metal dichalcogenides. *J. Appl. Phys.* **122**, 224302 (2017).